Article

Baroclinic Effect on Inner-Port Circulation in a Macro-Tidal Estuary: A Case Study of Incheon North Port, Korea

Jae-Soon Jeong [1], Seung-Buhm Woo [2],*, Han Soo Lee [1], Bon-Ho Gu [3], Jong Wook Kim [2] and Jin Il Song [2]

[1] Transdisciplinary Science and Engineering Program, Graduate School of Advanced Science and Engineering, Hiroshima University, 1-5-1 Kagamiyama, Higashi-Hiroshima 739-8529, Japan; jeong.jaesoon93@gmail.com (J.-S.J.); leehs@hiroshima-u.ac.jp (H.S.L.)

[2] Department of Ocean Science, Inha University, Incheon 22212, Korea; kaonesis@gmail.com (J.W.K.); jisong855@mpl.inha.ac.kr (J.I.S.)

[3] Marine Disaster Research Center, Korea Institute of Ocean Science and Technology, Busan 49111, Korea; bhgu@kiost.ac.kr

* Correspondence: sbwoo@inha.ac.kr

Abstract: This study investigated the flow patterns and affecting factors in the North Port of Incheon, South Korea, to understand the inner-port circulation characteristics by applying an unstructured grid finite volume community ocean model (FVCOM) together with a field survey. The FVCOM considered the tide, river discharge, surface winds, and atmospheric pressure with the highest resolution of 50 m around the port. The model results were validated with current velocity and salinity observations. In the main channel, the difference in salinity between the sea surface and bottom increased during the neap tide due to weakened tidal currents, thus strengthening the stratification. However, at the inner port, strong stratification was observed during spring tide as the near-surface freshwater from upstream of the estuary moved relatively farther south of the port than that during the neap tide. Freshwater flowed into the port during the flood current and was trapped in the semi-closed geometry of the inner port. The horizontal salinity gradient between the trapped fresher water in the port and saltier water in the main channel increased during the flood current. As a result, density-driven circulations associated with near-bed currents towards the port were maintained for more than 3 h after high tide. This result implies that the baroclinic effect, mainly due to the salinity gradient in the North Port, could significantly affect residual circulation at the inner harbor in a macro-tidal environment and the mass transport mechanism, such as sediment transport. In general, such enhanced baroclinic effects due to salinity and tides are not limited to the North Port and can have greater effects on inner-port circulation in other macro-tidal harbors that suffer from severe sedimentation problems.

Keywords: density-driven circulation; stratification; sediment deposition; FVCOM; Gyeonggi Bay

1. Introduction

In a port where seawater circulation is stagnant, problems such as degradation of water quality and sedimentation may occur. If circulation stagnation in a port causes heavy sedimentation, the water depth in the port becomes shallow, and thus continuous dredging is required. Human activities, such as channel deepening and dredging, can alter the natural tidal dynamics, which can also cause local sediment transport [1,2]. Many studies have been conducted to determine the main reasons for sedimentation using measurement data or numerical models to reduce sedimentation problems in estuaries [3–5]. It is essential to understand circulation around the port to determine these sedimentation factors.

Most ports are located in estuaries, and it is necessary to study estuarine circulation to understand the circulation around the port, which is mainly driven by barotropic and baroclinic pressure forces. In a macrotidal estuary, a strong tidal current is generated by the barotropic force caused by a large horizontal sea surface gradient. In contrast, in

estuaries with large river discharges, strong two-layer circulation can be generated by the baroclinic force caused by a horizontal salinity gradient between freshwater and seawater and originating from land.

The two main forces at the estuary (barotropic and baroclinic forces) contribute the most to the inner-port circulation. In a port where the mouth is located at a right angle to the main channel, water circulation can be interpreted as the superposition of three types of flows: barotropic inflow and outflow by the tide; eddy around the entrance of the port due to tidal current; baroclinic vertical circulation by the density difference between the inside and outside of the port [6]. Among these flows, curl, introduced into the port following topography, tends to become the center of sedimentation in the port [7]. From a tank experiment, areas with high sedimentation were matched with those with high mean vorticity calculated from the time-averaged velocity [8].

Most of these studies are mainly observation-based, helping significantly in understanding and analyzing physical mechanisms. However, due to the spatiotemporal limitations of measurements, it is also important to analyze spatiotemporal changes in seawater circulation through numerical modeling. Unstructured numerical models, which have recently received considerable attention, have various advantages, such as the efficient reproduction of complex coastlines and high-resolution grids around the study area of interest. Recently, these unstructured ocean models have been applied to the study of port circulation.

The North Port of Incheon in Gyeonggi Bay, located in the central part of the west coast of Korea, is perpendicular to the main channel, and the length of the port is 3.2 km. The overall sedimentation rate in the port is 64.2–100 cm/year at the entrance and 10 cm/year at the inner end of the port [9], indicating a spatially diverse distribution of deposition compared to its length scale. Due to the particularly high sedimentation rate at the entrance, dredging operations to maintain the water depth are steadily progressing for the safe navigation of vessels. As dredging operations are cost-intensive, there is an urgent requirement to understand the fundamental factors of sedimentation.

Previous studies around Gyeonggi Bay have focused primarily on hydrodynamic and salt behavior around the main channels [10–12]. In other studies focused on the North Port, current fields also showed an anticlockwise curl at the port entrance during flood tide. The characteristics of the sediment dynamics were studied by focusing only on the barotropic flow by the tide and the curl generated at the port entrance. In the port, the tide increases up to 9 m during spring tides; river discharge has increased up to 12,000 m^3/s during the flood season for the last 20 years. Considering the tidal range and river discharge, it is necessary to address the barotropic and baroclinic effects on the current fields and sedimentation.

Therefore, the objective of this study was to investigate and understand the physical mechanisms behind circulation and sedimentation using observations and numerical models. An unstructured grid numerical model was attempted for the first time at this port by applying a high-resolution grid with a maximum resolution of 50 m. The effect of freshwater flowing into the North Port on the baroclinic vertical circulation and the residual flow in the port were investigated and validated with field observations. This study can help investigate one of the reasons for sedimentation and understand the reasons for the high tendency of sedimentation in the port.

2. Materials and Methods

2.1. Study Area

The study area, located in the central part of Gyeonggi Bay on the west coast of the Korean Peninsula, contains many islands (Figure 1a). In Gyeonggi Bay, a wide range of intertidal zones is formed, with the topography over 50 m deep in the open sea. As the tides approach inland, they become less than 10 m deep in most coastal areas, except for waterways (Figure 1b). The main islands of Gyeonggi Bay are Yeongjong and Ganghwa. The main channel, the Yeomha Waterway, is a meridional waterway approximately 20 km in length on the right side of Ganghwa Island. Freshwater from the Han, Imjin, and

Yesung Rivers flows to the north port via the Yeomha Waterway. The North Port is situated perpendicular to the main channel with a port of 3.2 km east–west and 1 km north–south (Figure 1c). The main channel is approximately 20 m deep, and the depth of the port was maintained at approximately 10 m by dredging.
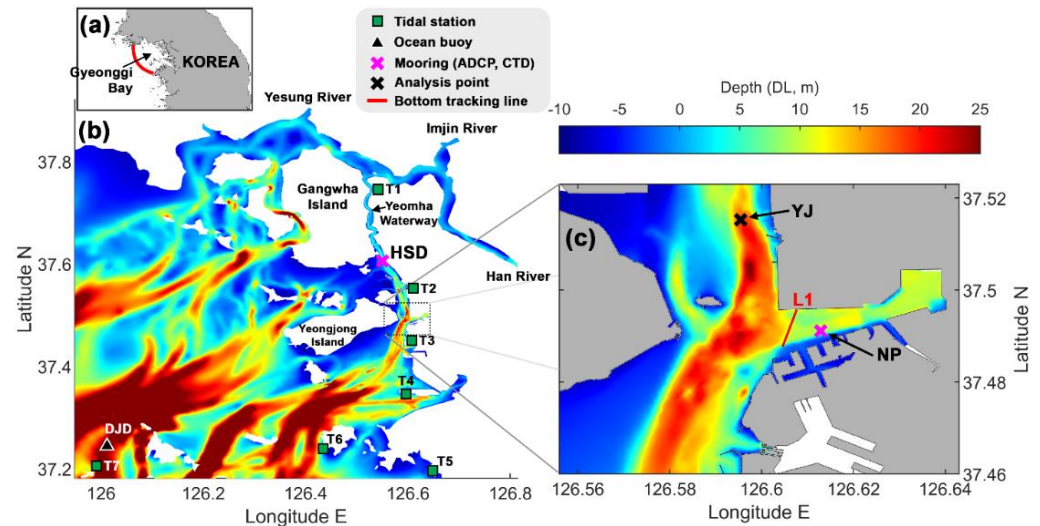
Figure 1. (**a**) Part of the Korean Peninsula; (**b**) Gyeonggi Bay and observation sites; (**c**) the North Port and its bathymetry. HSD (Hwangsan-Do) and NP (North Port) indicate locations of acoustic doppler current profiler (ADCP) observation. DJD (Deokjeok-Do) indicates an ocean buoy observation site.

2.2. Field Surveys and Data Collection

As seen in Figure 1, two moorings were deployed to verify the seasonal variability of currents and salinity: one at the southern end of the Yeomha Waterway, named HSD (126°32.91′ E, 37°36.94′ N) (Figure 1b); the other at the inner North Port, named NP (126°36.79′ E, 37°29.46′ N) (Figure 1c). Surveys were conducted during winter for 33 days, from 11 February to 15 March, and in summer for 36 days, from 24 July to 28 August 2019. At the mooring points, flow velocity with acoustic Doppler current profilers (ADCPs) and temperature and salinity at the surface and bottom layers with individual conductivity-temperature-depth (CTD) sensors were observed. ADCP sensors, fixed to trawl-resistant bottom mount (TRBM) frames on the sea bottom, were directed upward for bottom-up observations. The bottom CTD sensor was installed at the edge of the frame, and the surface CTD sensor was placed approximately 4 m below the sea surface. Appendix A presents the measurement instruments information in Table A1.

On 8 August 2019, observations were conducted along L1 in Figure 1c with 1 h intervals for 13 h from 8:40 to 19:40 using a ship-bottom-mounted ADCP, installed on a frame fixed to the side of the ship in the bottom tracking mode and placed 1 m below the water surface. See Appendix A for details of the instrument.

Hourly tide data from seven tide stations were collected from the Korea Hydrographic and Oceanographic Agency (KHOA) (Figure 1b). Observations, such as surface winds, pressure, and waves, were also collected from an ocean data buoy at the Deokjeok-Do (DJD) from the Korea Meteorological Administration (Figure 1b). Significant wave height data were then used to validate the wind-wave model results.

2.3. Physical Environment

The major external forces considered in this study area were freshwater inflow from the river mouth, tides at the open boundary, and surface winds. For freshwater inflow, the time series of river discharge from the Han River in 2019 is presented as a black line in Figure 2a. The 95 percentile value was calculated using two decades of data of freshwater flowing from the Han River, and the range within it was painted gray (Figure 2a). For tides

and winds, the entire year was not presented; however, winter and summer were presented by expanding the study period (Figure 2b,c). The expanded period is shown in Figure 2a.
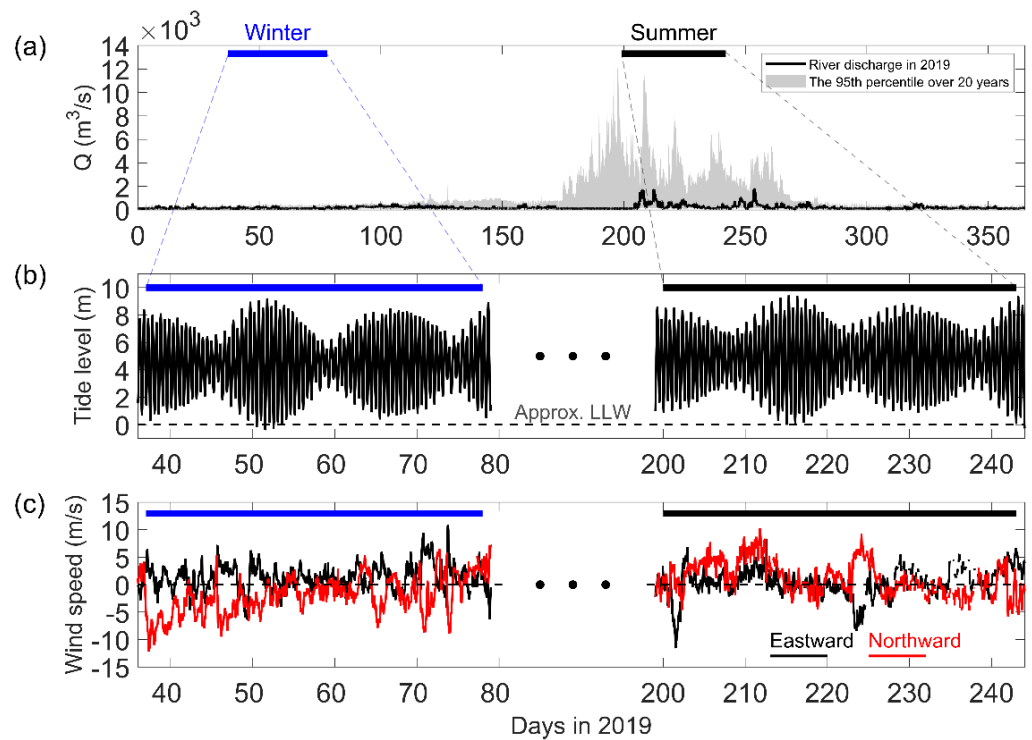
Figure 2. Observed data used in the study. (**a**) Annual River discharges. Two bars (winter and summer) indicate simulation periods of the FVCOM model; (**b**) observed tide at T3; and (**c**) observed wind speed at DJD ocean buoy.

During the rainy season in summer, freshwater intensively flows out of the Han River in July–September, reaching approximately 12,000 m^3/s. In other seasons, a small amount of freshwater (approximately 200 m^3/s or less) flowed out of the river (Figure 2a). During the study period in 2019, approximately 2000 m^3/s of freshwater flowed out in the summer, relatively low compared to other years.

The maximum tidal range is approximately 9 m during spring tide, and the minimum is approximately 2 m during the neap tide, thus characterizing the study region as a macro-tidal environment with great variability between spring and neap tides (Figure 2b). The harmonic constants observed in 2019 at the Incheon tidal station, closest to the North Port, are listed in Table 1. The data show that the semidiurnal tide is dominant with the amplitudes of M_2 and S_2 as 282.3 and 113.5 cm, respectively.

Table 1. Observed harmonic constants in 2019 at the Incheon tidal station.

	M_2	S_2	K_1	O_1	N_2	L_2	Q_1	MU_2
Amplitude (cm)	282.3	113.5	38.9	28.9	52.5	15.0	4.7	9.4
Phase (°)	129.5	186.1	303.2	263.4	108.4	148.8	238.7	178.3

As a result of the interaction between tide and river discharge, the spatial extension of salinity intrusion changes in most estuaries [13]. Between the river discharge Q and the length of salinity intrusion L, power-law relations with diverse exponents have been proposed in the form of $L–Q^N$, where N can vary from $-1/2$ to $-1/7$ for high to low river discharge [14–17]. Even in the same estuary, the value of N can vary due to the amount of river discharge, demonstrating that salt intrusion decreases as river discharge increases by a power law [18]. In the case of Gyeonggi Bay, the study area, the power-law

regression showed $L \sim Q^{-1.6/10}$ at the Yeomha Waterway, the main channel [19]. The Yeomha Waterway showed a similar tendency of salt intrusion related to river discharge as other estuaries in previous studies [14–17].

Tides can also transform the distribution of salt intrusions. During the neaps, with weakened vertical mixing, the enhanced salt intrusion moved further into the river [15]. Between tidal current, U_t, and the length of salt intrusion, L, power-law relations with diverse exponents also have been proposed in the form of $L \sim U_t^N$, where N can vary from −0.86 to −0.36 by topography, river discharge, etc. [17,20]. These results indicate that salt intrusion tends to be inversely proportional to the magnitude of the tide and the amount of river discharge in this estuary.

In 2019, seawater density was observed using the surface and bottom CTD data at HSD and NP, as illustrated in the TS diagram (Figure 3). As the water depth in the study area was shallow, the effect of pressure on density was excluded. Seawater density varied in the range of approximately 1020 kg m^{-3} in winter and 1010 kg m^{-3} in summer. In both summer and winter, it was confirmed that the seawater density in the study region depended strongly on the variation in salinity rather than the temperature variation. In summer, due to the large river discharge, the density varies between 1000 and 1020 kg m^{-3}. Moreover, in both seasons, the density difference between the main channel (HSD) and the port (NP) was significant, mainly due to the salinity variation. Thus, in this study, the results of the summer season, with greater density variability, were analyzed and discussed.
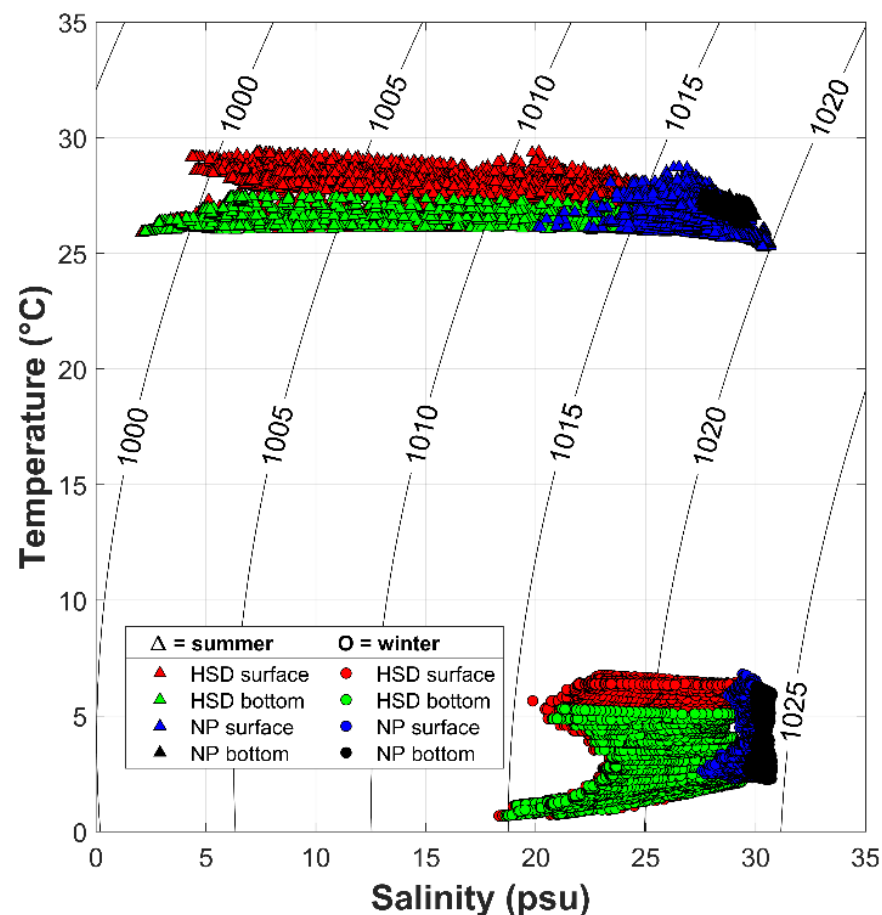
Figure 3. Temperature/salinity (TS) diagram using Conductivity, Temperature, Depth (CTD) observations at HSD and NP in winter (11 February–15 March 2019) and summer (24 July–29 August 2019).

2.4. Numerical Model

In this study, we used an unstructured grid ocean circulation model—the finite-volume coastal ocean model (FVCOM). The governing equations of FVCOM consist of the following continuity, motion, and heat–salt conservation equations [21,22].

$$\frac{\partial u}{\partial x} + \frac{\partial v}{\partial y} + \frac{\partial w}{\partial z} = 0, \tag{1}$$

$$\frac{\partial u}{\partial t} + u\frac{\partial u}{\partial x} + v\frac{\partial u}{\partial y} + w\frac{\partial u}{\partial z} - fv = -\frac{1}{\rho_0}\frac{\partial P}{\partial x} + \frac{\partial}{\partial z}\left(K_m\frac{\partial u}{\partial z}\right) + D_u, \tag{2}$$

$$\frac{\partial v}{\partial t} + u\frac{\partial v}{\partial x} + v\frac{\partial v}{\partial y} + w\frac{\partial v}{\partial z} + fu = -\frac{1}{\rho_0}\frac{\partial P}{\partial y} + \frac{\partial}{\partial z}\left(K_m\frac{\partial v}{\partial z}\right) + D_v, \tag{3}$$

$$\frac{\partial P}{\partial z} = -\rho g, \tag{4}$$

$$\frac{\partial T}{\partial t} + u\frac{\partial T}{\partial x} + v\frac{\partial T}{\partial y} + w\frac{\partial T}{\partial z} = \frac{\partial}{\partial z}\left(K_h\frac{\partial T}{\partial z}\right) + D_T, \tag{5}$$

$$\frac{\partial S}{\partial t} + u\frac{\partial S}{\partial x} + v\frac{\partial S}{\partial y} + w\frac{\partial S}{\partial z} = \frac{\partial}{\partial z}\left(K_h\frac{\partial S}{\partial z}\right) + D_S \tag{6}$$

where u, v, and w are the velocity components in the x-, y-, and z-axes; T and S are the water temperature and salinity; ρ and P denote density and pressure; f and g denote the Coriolis parameter and gravitational acceleration; K_m and K_h represent the vertical eddy viscosity coefficient and thermal vertical eddy diffusion coefficient, respectively; D_u, D_v, D_T, and D_S are the horizontal momentum and heat–salt diffusion terms, respectively. The FVCOM adopts the finite volume method, calculating the flux in triangular grids by differentiating the governing equations in the form of integrals. In addition, the equation of motion is calculated using the mode-splitting method. In the 3D internal model, the baroclinic flow was calculated using the second-order Runge–Kutta time-stepping method, and in the 2D external mode, the barotropic flow was calculated using the fourth-order Runge–Kutta time-stepping method. A detailed description can be found in [21,23].

2.4.1. Model Grids

The lengths of the model domain are approximately 150 and 135 km in the east–west and north–south directions, respectively. The open boundary was approximately 105 km west of North Port, as indicated by the red line in Figure 1a. A river source from the Han River, where the largest amount of freshwater flows, is approximately 100 km from the port along complicated coastlines. The grid consisted of 59,757 nodes and 113,918 cells, and the vertical grid was divided into 20 layers using a sigma coordinate system. Considering that the horizontal and vertical widths of the North Port are 3.2 km and 1 km, respectively, an unstructured grid was generated with a high resolution of 50 m to reproduce the flow patterns in the North Port. Due to the numerical instability of the coupled-wave model, it was impossible to run the model with a resolution higher than 50 m in this study (Figure A1). Near the open boundary, the grid size increased to approximately 4500 m. The depth data, referred to as mean sea level (MSL), were constructed using the latest data provided by the Korea Hydrographic and Oceanography Agency (KHOA).

2.4.2. Boundary Conditions and Initial Fields

For tides at the open boundary, harmonic constants M_2, S_2, K_1, O_1, N_2, L_2, Q_1, and Mu_2 were input. M_2, S_2, K_1, O_1, N_2, and Q_1 were obtained from the TPX08-atlas global tidal model (1/30-degree resolution) [24]. By harmonic analysis of the elevation from the Incheon tide station, L_2 and Mu_2 were added. For salinity data at the boundary, we used the series of oceanographic observation data provided by the National Institute of Fisheries Science. These data were recorded every year in January, March, May, July, September, and

November at 207 points across the country. Among these observation points, the salinity data from the point closest to the open boundary of the model were interpolated and input into the model.

For freshwater discharge data, hourly data from the Paldang Dam, provided by the Han River Flood Control Center, were used. Discharges of 30% and 15% of the Paldang Dam were inputted as the discharge data at the Imjin River and Yesung River, respectively, as observational data were not available for them [10]. We simulated the model with freshwater discharge for two years to obtain an initial field of salinity. The result of the model was used as the initial field of salinity, facilitating the usage of a sufficiently mixed salinity field for Gyeonggi Bay.

For atmospheric forcing, U10, V10, and atmospheric pressure data were inputted from the Local Data Assimilation and Prediction System (LDAPS), an atmospheric model of the Korea Meteorological Administration. The LDAPS receives the boundary field from the global model, makes a new prediction every 3 h, and provides a model result dataset every 3 h. The 0, 1, and 2 h results of each model result dataset were combined to form atmospheric fields with an interval of 1 h.

The bottom roughness length (z_0) used near the bottom boundary may vary depending on the composition of the seabed or water depth [25]. These values were considered differently depending on the depth of water, as suggested in a previous study [26].

$$z_0^b = \begin{cases} 3 \times 10^{-3} & if \ D \leq 40 \\ 3 \times 10^{-3} \ \exp^{-(D-40)/8.8204} & if \ 40 < D \leq 70 \\ 1 \times 10^{-4} \ \exp^{-(D-70)/13.0288} & if \ 70 < D \leq 100 \\ 1 \times 10^{-5} & if \ D > 100 \end{cases} \tag{7}$$

2.4.3. FVCOM-SWAVE

In wave models, source terms for wind-wave dynamics, such as wave growth [27], whitecapping [27], and energy dissipation due to bottom friction [28], depend mainly on empirical formulas. Empirical equations and constants were selected to simulate each phenomenon in an unstructured grid finite-volume surface wave model (FVCOM-SWAVE) [29]. The horizontal grid used in the wave model was the same as that used in the ocean model. The results obtained by simulating only the wave model without the ocean model were inputted to the ocean model (one way).
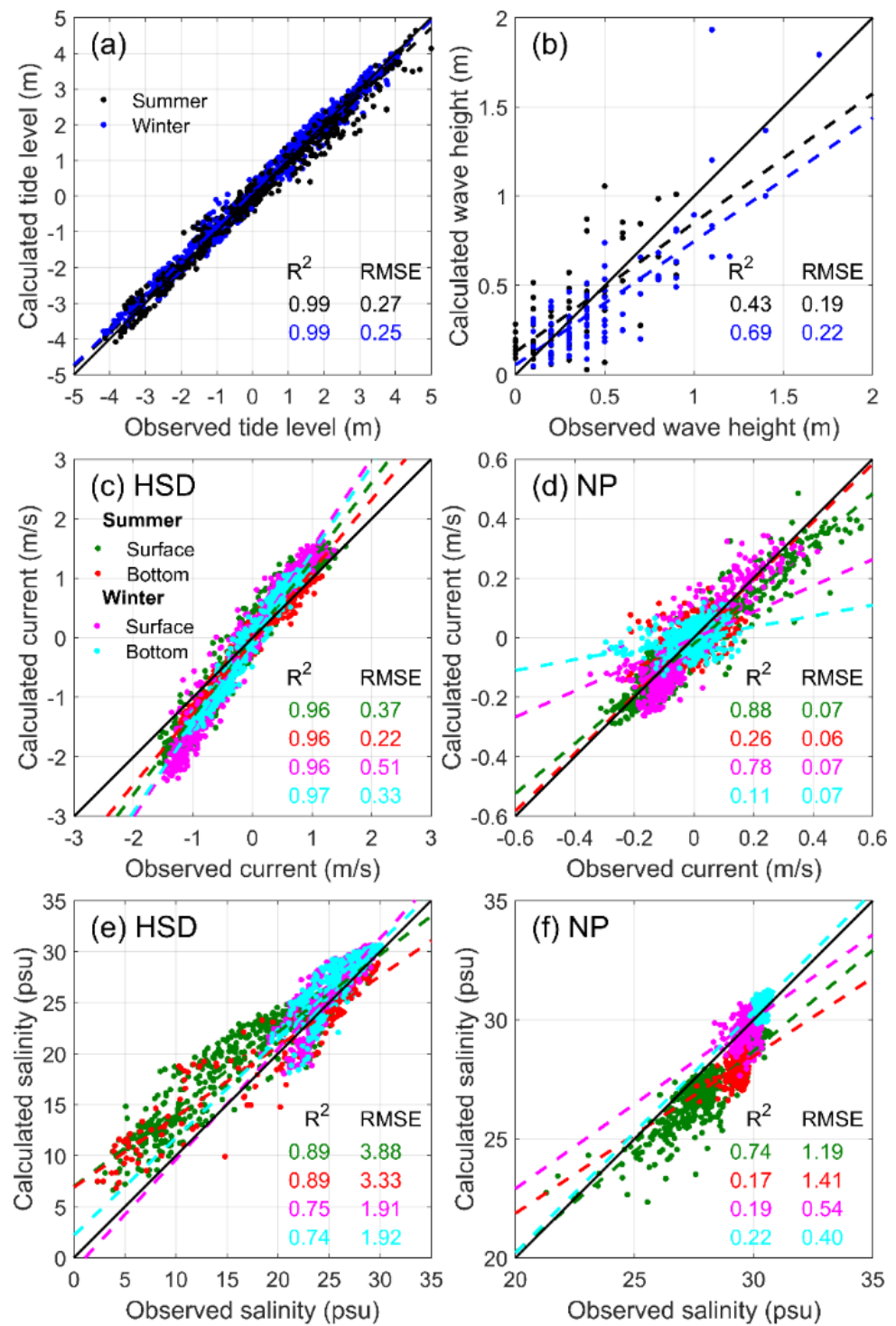
3. Results

3.1. Validation

A comparison between the calculated and observed values for tide level, current velocity, and salinity concentrations at the HSD and NP sites in summer and winter is shown in Figure 4. For the tide elevation, the R^2 of each season was calculated by averaging the R^2 values of the seven tide stations (Figure 4a).

For flow velocity, the V component was verified in the main channel because the channel was formed in the north–south direction; the U component was verified in the North Port developed in the east–west direction. As the flow velocity and salinity data were observed at the surface and bottom layers, including two seasons, four spatially and temporally different datasets were obtained from each station. Each of these four data points was statistically analyzed.

The tide elevations in both seasons showed high correlations, and the significant wave height showed high reproducibility in winter. The observed tidal amplitudes in Gyeonggi Bay were 8 m or more during spring tides, sufficiently reproduced in the model with high R^2 values of 0.99 (Figure 4a). In the case of wave heights, the range of variation was wider in winter than in summer because of the high waves formed by strong northwest winds. Although the model underestimated the observation, the R^2 value for waves in winter was 0.69 and sufficiently well reproduced (Figure 4b).

Figure 4. Comparison between observations and the model results. (**a**) Tide levels at 7 stations; (**b**) significant wave heights at DJD; (**c**,**d**) velocities observed from ADCP at HSD and NP; and (**e**,**f**) Salinity observed from CTD at HSD and NP.

At the surface layer, stronger velocities were observed in both the main channel and North Port, and the model showed similar patterns (Figure 4c,d). In both seasons, the surface and bottom velocities in the main channel showed a maximum of 1.5 and 1.2 m/s, respectively. In contrast, the velocity in North Port was relatively less and showed seasonal differences. In summer, the positive velocity currents toward the port were observed to be more than 0.5 m/s at the surface layer, but the outflow velocity was observed to

be weaker at −0.3 m/s, indicating that strong inflow occurred during flood tides and relatively weak outflow occurred during ebb tides. In winter, the positive velocity showed a maximum of 0.4 m/s, lesser than that in summer. This asymmetry between the surface inflow and outflow was well reproduced in the model (R^2 of 0.88 and 0.78 in summer and winter, respectively). The inflow and outflow at the bottom layer were observed to be approximately within 0.2 m/s in the port; the variations were smaller than those at the surface layer due to the relatively poor performance of the model.

In the case of salinity in the main channel, the variance varied from 2–30 psu depending on the tide in summer. Although the calculated salinity was generally higher than the observed salinity, the trend was sufficiently well reproduced with an R^2 of 0.89 (Figure 4e). The salinity in winter was 18 psu, not dropping to 2 psu as in the summer; this was also well reproduced in the model (R^2 = 0.75 and 0.74 at the surface and bottom layers, respectively). However, the salinity in the North Port varied in a much shorter range than that of the main channel. Except for the surface salinity in summer, the salinity exhibited a variance of approximately 2 psu even during the spring tide (Figure 4f). Although the model result could not follow these small variances, the absolute values of salinity were similar between the model and observation (RMSE of 0.40 to 1.41 psu). In summer, the surface salinity dropped to 21 psu in the port, showing relatively large fluctuations; this pattern was also reproduced in the model (R^2 = 0.74).

3.2. Stratification by Salinity

The baroclinic force was induced by the spatial difference in the density of seawater, and salinity was the main determinant of this density in the study region, as illustrated by the TS diagram (Figure 3). The difference in salinity between the surface and bottom layers was compared with the observed data to verify whether the vertical salinity gradient was sufficiently reproduced in the model. By superimposing data from two seasons on one axis, the seasonal differences in vertical salinity and the fortnightly spring-neap tidal cycle were simultaneously compared. When the data were superimposed on one axis, the time series shifted to match the tidal phase. The time series of freshwater discharge and salinity also shifted corresponding to the tidal time series. Considering the vertical difference, the normalized value was obtained by dividing the maximum value from each observation by the model result (Figure 5c–f). Figure 5c,d were obtained from the observation and model results at HSD, Figure 5e,f were obtained at NP. In regions where salinity is dominant, the vertical salinity difference can be considered the strength of stratification, referred to as stratification in this study.

Stratification is favorable when tidal currents are weak. As the current is relatively weaker during the neap tide, stronger stratification generally develops during the neap tide; the same pattern was also observed in the HSD main channel. Although there were many missing data points, the stratification during the neap tide was stronger than that during the spring tide in both seasons (Figure 5c). In addition, in the model results at the same location, the vertical difference in salinity was larger during neap tide. The observations confirmed data only for 15–20 days, but the model results showed the nightly occurrence of this phenomenon.

Compared to the stratification during the neap tide at the main channel, a different pattern was observed and calculated for the North Port. The stratification developed in the port during the spring tide; it was weakened compared to that during the neap tide.

In the main waterway, stratification developed when tidal currents were weak. However, in the port, it developed when the tidal currents were strong, showing opposite phases with stratification in the main waterway. In this pattern, the intensity of the stratification may be slightly stronger or weaker as the freshwater inflow increases or decreases, but the variability of the 15-day cycle, which is a period of spring and neap tides, is dominant. A phenomenon different from the general mechanism of stratification occurs in the North Port, appearing the same in both the observation and model during summer and winter.
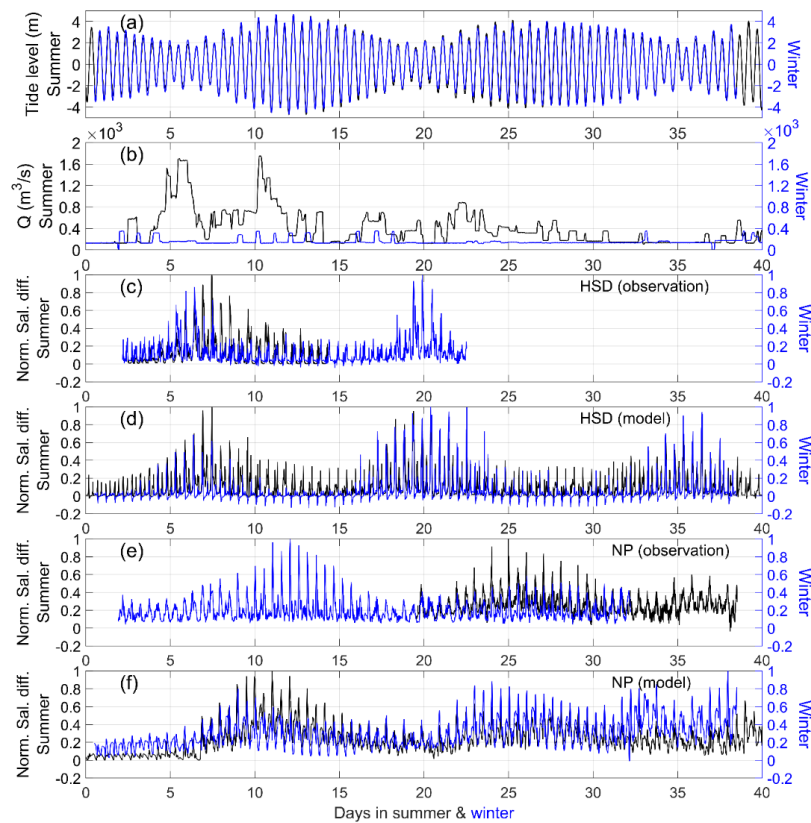
Figure 5. Normalized salinity differences between surface and bottom at HSD and NP, calculated from CTD data and model results. (**a**) Tides; (**b**) river discharge; (**c**,**d**) observed (calculated) salinity differences at HSD; and (**e**,**f**) observed (calculated) salinity differences at NP.

3.3. Cross-Sectional Net Velocity of the Port

The velocity data observed in the tracking mode of the ADCP were used as verification data to verify whether the current velocities flowing in and out of the North Port were properly reproduced. Using the ADCP tracking 13 h data crossing the North Port, the surface and bottom net velocities passing the cross-section of the port were calculated and compared with the model results (Figure 6). The track line is indicated by the red line in Figure 7a.
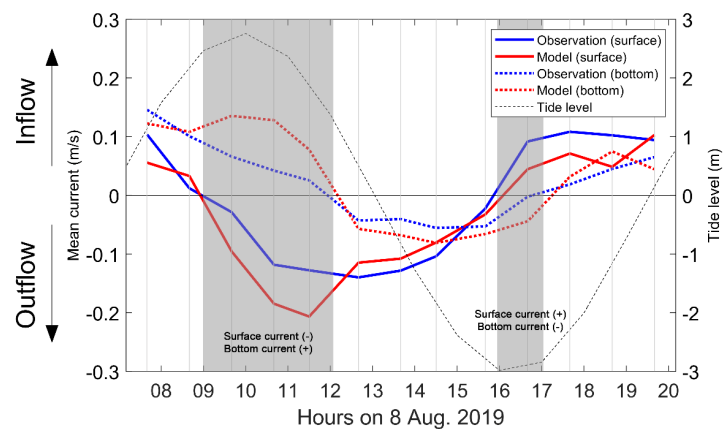
Figure 6. Spatially averaged currents across the North Port. Positive (negative) currents indicate flows toward (away from) the port. The gray vertical lines indicate the time at which the observation was conducted. The gray shades indicate the periods when the directions of the surface and bottom currents were reversed.
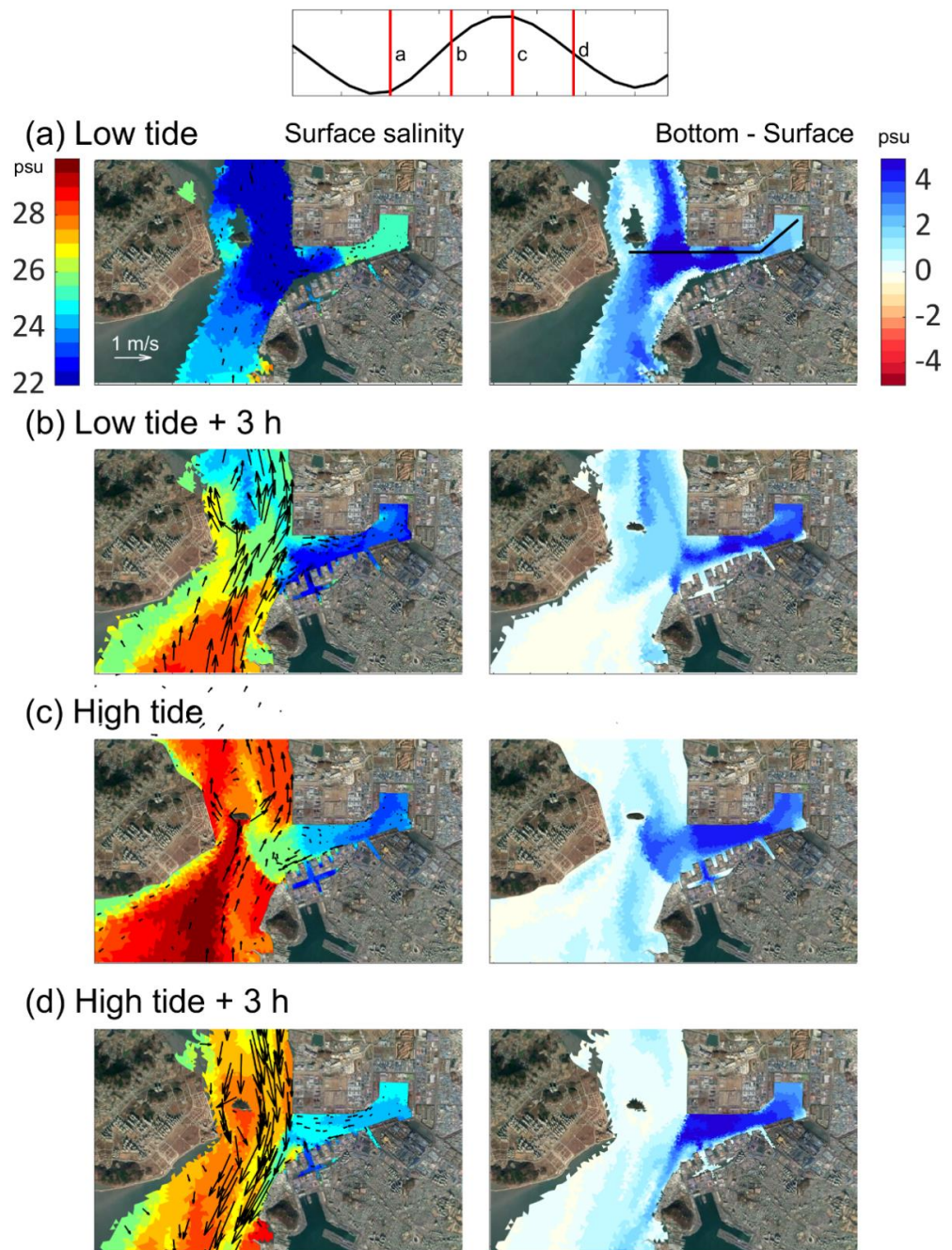
Figure 7. Spatial distributions of depth-averaged velocity and surface salinity (**left**) and vertical salinity difference (**right**) from the model results in summer under high river discharge conditions. Positive value (blue shades) in the salinity difference means that surface seawater is fresher than bottom water.

After high tide, the ebb tide lowered the tide elevation. The relationship between the tide elevation and tidal current was well observed for the surface net velocity in the North Port. The model results showed a trend similar to that of the observation results. Both the observation and model showed an ebb current (negative) from 09:00 (KST), and the current was converted to a flood current (positive) around 16:00. The magnitude of the surface current in the model was overestimated from 09:00 to 12:30 compared to the observations and was underestimated for the other times. The model sufficiently simulated the phase of the current according to the tide.

Although the magnitude of the bottom net velocity was underestimated in the model, the phase of the current followed the phase from the observation. It should be noted that the duration of the flood current was 3 h longer than that of the ebb current in the bottom layer. During the entire observation tracking duration of 13 h, ebb currents were observed for only 5 h, and flood currents were observed for another 8 h. Similarly, in the model, the same duration of ebb and flood currents were calculated. The reason for this asymmetry is that the bottom current into the port continued until 12:00, when the tidal elevation decreased after the high tide. After 12:00, the direction of the currents changed to the ebb tide, and it continued until the low tide at 16:30, but immediately changed to the inflow direction due to the next flood tide.

Comparing the surface and bottom net velocities, the bottom velocity responded 3 h later at ebb tide after high tide, whereas the 3 h difference was reduced to 1 h at flood tide after low tide. The biggest cause of this asymmetry was the velocity in the flood direction at the bottom layer, which was maintained even during the ebb tide. In addition to the duration, the magnitude of the current is asymmetric. In the surface layer, the maximum magnitude of the ebb current is greater than that of the flood current. In contrast, in the lower layer, the maximum magnitude of the flood current is greater than that of the ebb current. Therefore, the residual current, calculated by averaging the 13 h of data, showed a residual outflow of the surface current and a residual inflow of the bottom current.

4. Discussion

4.1. Spatial Distributions of Salinity

As shown in Figure 5, the diurnal variability of the stratification in the northern part was greater during the spring tide than the neap tide. In addition, in Figure 6, the inflow and outflow durations of the surface net velocity were observed symmetrically at 6 h. In the bottom layer, the inflow duration was 2 h longer than the outflow duration, showing an asymmetrical tendency. Based on the results of the stratification and cross-sectional net velocities in the port, a velocity shear due to the current difference between the surface and bottom occurs when the stratification develops in the port during the spring tide.

The spatial salinity distribution was analyzed to discuss the relationship between salinity-driven stratification and flow velocity near the North Port. Figure 7 presents the surface salinity distribution and salinity differences between the surface and bottom at low tide, low tide +3 h, high tide, and high tide +3 h. These four specific times in the tidal cycle were chosen as the periods in which a large amount of freshwater flowed during the spring tide in the summer model. The blue shades in the right panel of Figure 7 indicate that the surface seawater is fresher than the bottom seawater and that the stratification is stronger.

At low tide, a surface salinity of 22 psu and a salinity difference of 4 psu were calculated at the main waterway in front of North Port (Figure 7a) as the surface low-salt water from the Han River flows into the sea off the North Port during the ebb tide. However, the innermost surface salinity of the port was 25 psu, higher than that of the main channel, and the salinity difference was 2 psu; therefore, stratification was weaker.

Stratified freshwater in front of the port flowed into the port via flood tides (Figure 7b). Consequently, the inner salinity decreased by 2 psu from 25 to 23 psu, and the stratification was further strengthened. The incoming seawater was trapped in the port, maintaining lower salinity and strengthening stratification, even as the flood tides continued. However, the salinity of the seawater in the main channel continued to increase due to the high-salinity water flowing along the upstream channel with the tide, weakening the stratification. This caused the horizontal gradient of salinity between the port interior (low salinity) and main channel (high salinity) to increase as the floods progressed.

At high tide, the salinity in the port increased slightly, but it still maintained a low salinity due to its isolation. Conversely, the salinity of the main channel rose steadily to 29 psu, and the horizontal salinity gradient increased to 6 psu, with the maximum salinity front at high tide between the isolated seawater in the port and high-salt water outside (Figure 7c). In other words, while the salinity changed rapidly in the main channel

depending on the flood/ebb tide, the salinity in the port could not react rapidly because of the trapped seawater. This difference in the reaction rate caused an abnormally strong salinity front between the main channel and port.

Ebb currents increase the salinity of the surface layer by draining surface seawater from the port into the main channel. As a result, the surface salinity rose by 1 psu. At the main channel, the salinity was reduced by 1 psu due to the freshwater coming from upstream, thus reducing the horizontal salinity gradient between the main channel and port. Although the horizontal front was weakened, the strength of the vertical stratification was stronger at the port entrance, which had the strongest stratification compared to those at other times (Figure 7d). Overall, at all tide times, the stratification in the port was stronger than that in the main channel. Then, when the low tide started again, the fresher water from the upstream came down to the front of the North Port, and the process of spatial salinity distribution in Figure 7 was repeated.

The phase difference in the salinity change between floods and high tides develops a salinity front. A greater salinity front can develop in the case of greater tidal forces and freshwater inflow. Moreover, the spring tide with the largest tidal range is a favorable condition for the development of the front, but this phenomenon does not always occur during the neap tide. Even though the tidal range is low, the isolation of seawater in the port is unavoidable because of the geometric and geographical environment, and the phase difference between the main channel and port is inevitable.

4.2. Along-Port Cross-Sectional Salinity and Current Profile

A strong salinity front was observed between the main channel and harbor in the horizontal salinity distribution. The baroclinic force created by the front creates currents that flow into the port at the lower layer and out of the port at the surface layer. In other words, when freshwater was in the right port and seawater was in the left main channel, denser water spread to the bottom and low-density water rose to the surface, causing a density-driven current. The flow velocity in most sea areas occurs in the form of an overlap between the density-driven current and current generated by the barotropic force of the tides.

Figure 8 illustrates the vertical density-driven current and salinity profile along the cross-section of the port (Figure 7a) at the same tidal times defined in Figure 7 to evaluate the effect of the baroclinic process on the flow velocity of each layer in the port.

As in Figure 7a,b, the freshwater from the upstream river during the ebb tide flowed into the port along the flood current, and the surface salinity decreased (Figure 8a,b). Relatively high seawater of 28 psu remained in the bottom layer, which cannot be confirmed in Figure 7. As the flood tide progressed, low-salinity water flowing into the port and high-salinity water at the bottom were mixed. Due to this mixing, the bottom salinity was lowered to 27 psu. Consequently, the salinities of the surface and bottom layers decreased, and the strength of the stratification in the port was maintained without variations.

At high tide, the salinity in the port was isolated; thus, it maintained a distribution similar to that shown in Figure 8b. However, in the case of the main channel, the surface salinity was approximately 28 psu, the bottom salinity was higher than 30 psu, and the salinity front developed to the maximum. The salinity front, developed to the maximum during the slack tide, induced a baroclinic pressure stronger than the barotropic pressure, causing a two-layer circulation structure of seawater in the port (Figure 8c). Accordingly, the high-salt water penetrated the port from the bottom layer and the low-salt water flowed out from the surface layer, forming a counterclockwise vertical circulation in the port.

At high tide +3 h, ebb currents are the strongest in the port, and seawater drains out of most of the port, but the current flows in the opposite direction only at the bottom layer (Figure 8d). Along this bottom countercurrent, high-salt water of 30 psu additionally flowed into the port, and the surface low-salt water flowed out from the bottom layer. The outflowing low-salinity water then flowed across the denser water near the port entrance. The origin of the bottom salinity flowing along the countercurrent was high-salinity water

from the open sea that flowed north upstream until high tide. Therefore, the stratification formed by the penetration of high-salinity water was stronger than that formed during other tidal times. The strength of the stratification increased to a maximum at the port entrance during the ebb tides, as shown in Figure 7d, explaining why a strong vertical difference in salinity was formed at the entrance to the North Port during ebb tides.
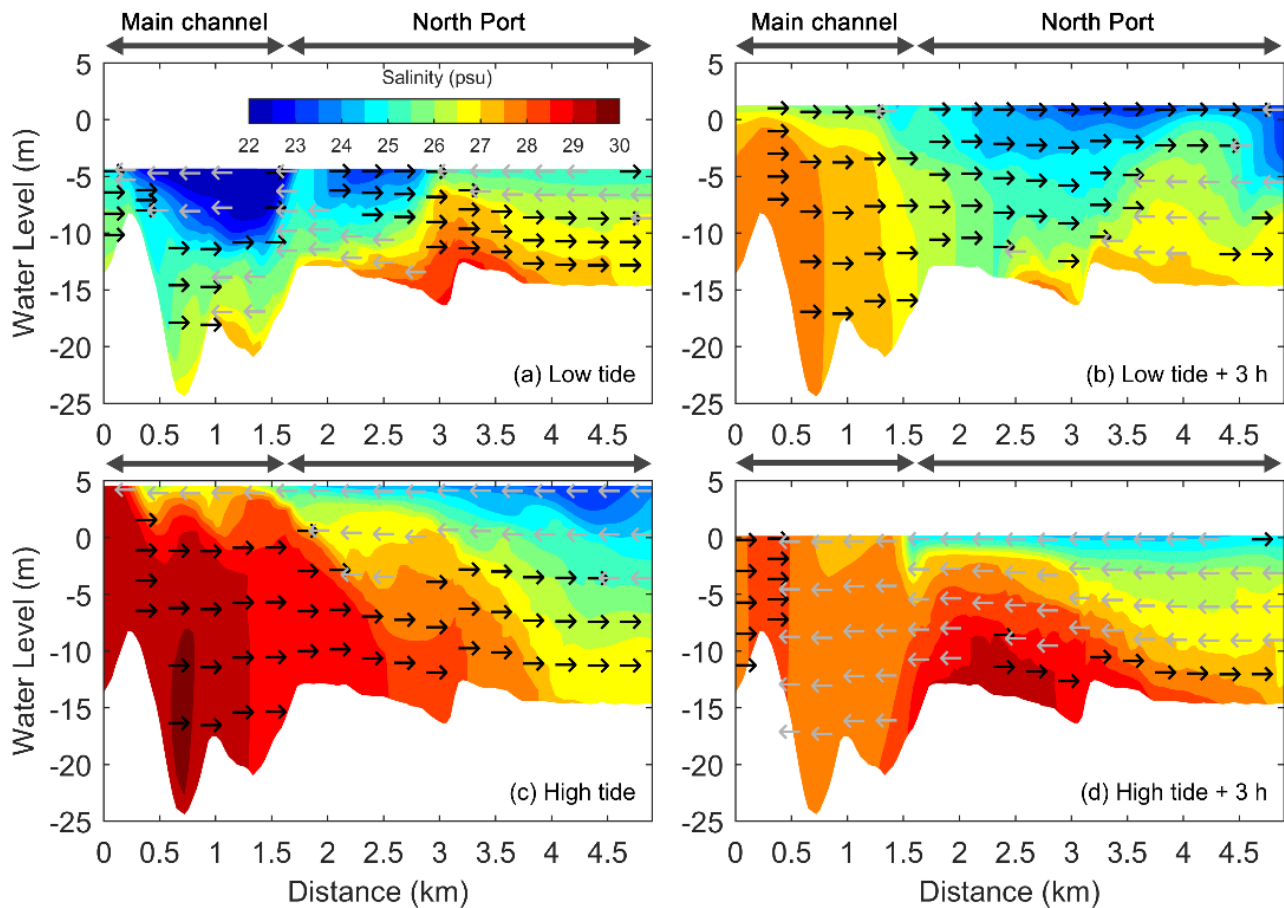
Figure 8. Along-port transects for the salinity profile and circulation from the model result at the same tidal time as defined in Figure 7. Vectors are unit vectors.

The difference in the reaction rate of horizontal salinity due to the high tide and topography causes a phase difference in the flow velocity between the surface and bottom of the port, thus causing the maximum development of stratification at the port entrance. The strong flow velocity and horizontal gradient of salinity in a macrotidal environment destabilize seawater, but the resulting stratification tends to stabilize it. In the following section, the process in the North Port is further investigated and discussed to identify the characteristics of inner-port circulation.

4.3. Inner-Port Stability by the Richardson Number

The Richardson number (Ri) is a dimensionless number accounting for the tendency of turbulent mixing. The denominator of Ri is the flow shear term, and the numerator indicates the buoyancy term. In the North Port, the strong flow velocity in the spring tides and the flow velocity induced by the horizontal salinity front increase the flow shear term, whereas the vertical stratification developing in the port increases the buoyancy term.

The Ri values at two points in the main channel, HSD and YJ, and one point in the port, NP, (Figure 1) were calculated and presented as a time series in Figure 9. The peaks of Ri in HSD and YJ are indicated by blue lines (Figure 9b,c) and the peaks at NP in the North Port are indicated by red lines (Figure 9d). A line with Ri = 1 is presented as a dotted line,

thus indicating the threshold value in this study for the seawater state between the vertical turbulent mixing prone condition (Ri < 1) and stable condition due to strong stratification (Ri > 1). In summer, the seawater temperature was considered constant at 27 °C in the calculation of Ri, as shown in Figure 3.
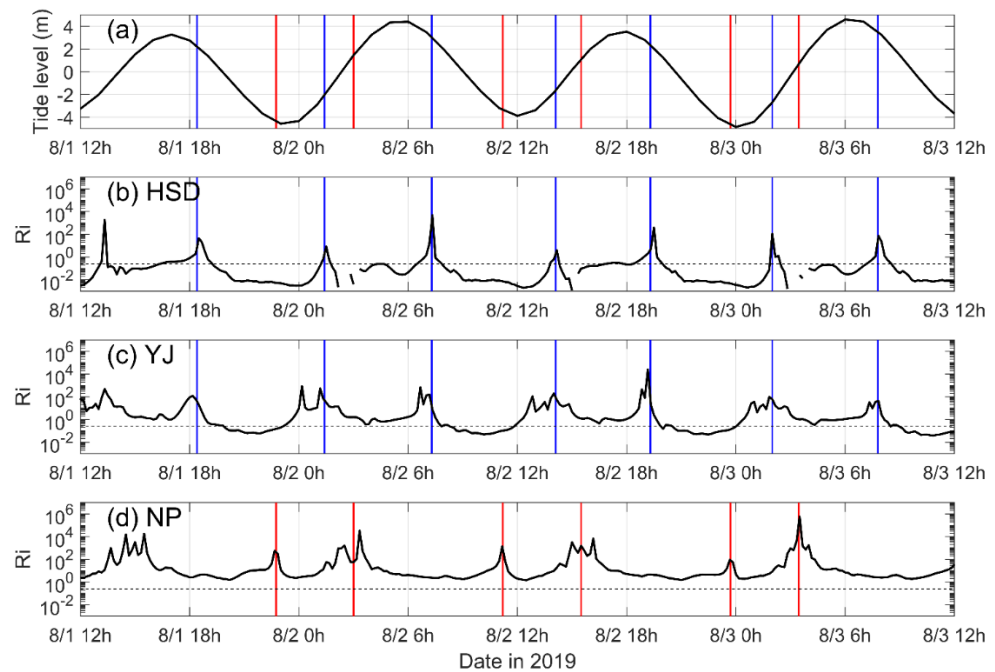
Figure 9. (**a**) Tide at T3, and Richardson numbers at (**b**) HSD; (**c**) YJ; and (**d**) NP, calculated from the model result (see Figure 1 for the locations). HSD and YJ are sited in the main channel while NP is in the port.

The peaks of Ri were calculated at high tide +1 h and low tide +1 h at both HSD and YJ, located in the main channel (Figure 9b,c). Although the two points were approximately 13 km apart, their peaks occurred almost simultaneously when the horizontal flow velocity was the weakest after one hour of slack tides. With a weakened flow velocity, the shear stress also decreased, resulting in a larger Ri; thus, the ocean became stable.

Although YJ and NP were located only 3 km apart, phase differences in Ri were observed. At NP, Ri peaks were calculated after the strongest flood tide. The increase in Ri after the floods implies that the floods had a greater effect on stabilization than the turbulence caused by the tidal currents in the North Port. The increase in Ri after the ebb tide indicates that the buoyancy effects induced by the saltier water flowing along the countercurrent were greater than the shear stress induced by the tidal currents in the surface layer and countercurrents in the bottom layer.

Although YJ and NP were more than six times closer than HSD and YJ, the absolute values also tended to be different, as the phases of Ri were different. Except for the time when Ri peaked in the main channel, Ri was higher inside the North Port because the speed of the currents inside the port was weaker than that in the main channel; conversely, the vertical stratification was strong. Therefore, if floating materials in the main channel flow into the stabilized port, they are unlikely to float longer and easily settle in the port.

5. Conclusions

Using field observations and numerical simulations focusing on the macro-tidal North Port, we analyzed the process of stratification development and its effect on two-layer circulation generation, especially during high discharge from adjacent rivers. We focused on the relationship between salinity and currents in and out of the port and attempted to distinguish the characteristics of in-port circulation from those in the main channel.

The salinity phase difference between the main channel and inner port is the main cause of baroclinic force generation. This phase difference was created because freshwater flowing south upstream during ebb tides entered and was trapped in the port during flood currents. The low salinity in the port was maintained because the trapped fresher water remained in the port until the next ebb tide started. Conversely, outside the port, the high-salinity seawater that flowed upstream through the main channel increased in salinity, making the salinity of the main channel the highest at high tide. Although the horizontal distance between the port and main channel was relatively short (approximately 3.5 km), the salinity difference increased to more than 4 psu at high tide, inducing a strong horizontal salinity gradient.

The baroclinic force induced by the salinity gradient caused a two-layer circulation in the port during the ebb tides. The strength of the force was strongest at high tide, whereas the magnitude of the tidal current was the weakest because it was close to the slack tide. This situation indicates a period in which the baroclinic force was greater than the barotropic force. The baroclinic force acting on the port was caused by low-salinity water in the inner port and high-salinity water in the main channel. This force caused the surface seawater to flow westward and the bottom seawater to the east, causing a vertical counterclockwise circulation in the port.

In a two-layer circulation caused by the strengthening of the baroclinic force, the inflow of high-salinity water into the port was strengthened at the bottom, and the near-bottom material could also be entrained with the flow. The two-layer circulation, which developed significantly during the spring tide, caused seawater inflow from the bottom to the port until the high tide +3 h. At this time, the bottom seawater was the most saline around the port because the seawater entered from the open sea and flowed upstream to the maximum tide level. Strong stratification was created at the entrance to the North Port by the inflow of the bottom seawater and the outflow of the surface-trapped seawater. Stratification at the port entrance made the seawater very stable, as depicted by a large Ri.

These results can be considered related to the sedimentation in this port. Due to the high sedimentation rate in the port, understanding the process of water circulation is essential to determine the reason for sedimentation. When seawater flows from the bottom, it can induce an influx of high-density substances, such as cohesive sediments, suspended in the bottom of the main channel. The suspended substances may sink after suddenly reaching a stable flow environment in the inner port area.

As a result, artificial structures, such as a current-deflecting wall (CDW), have been invented to prevent deposits of sediment in ports [7]. It is necessary to understand the natural systems to achieve efficient and successful management [29]. This research is the first study in the Gyeonggi Bay which shows the baroclinic effects on the inner-port circulation since most studies have focused on the dominant barotropic effect due to large tidal range. It revealed that even though macro-tides can enhance the baroclinic effect in harbors, the baroclinic effect due to the salinity gradient is relatively easier to ignore than the barotropic effect in macrotidal estuaries. This mechanism might not apply only to the North Port, but must also be considered as one of the factors causing severe sedimentation in other macro-tidal harbors.

Institutional Review Board Statement: Not applicable.

Informed Consent Statement: Not applicable.

Appendix A. Measuring Instruments

Table A1. Measuring instruments used in winter and summer.

	Winter		Summer	
	ADCP	**CTD (Surface, Bottom)**	**ADCP**	**CTD (Surface, Bottom)**
HSD	WorkHorse Sentinel 1200 khz, RDI	RBR virtuoso, IDRONAUT	Signature	XR-420, IDRONAUT
NP	WorkHorse Sentinel 600 khz, RDI	RBR concerto, IDRONAUT	WorkHorse Sentinel 1200 khz, RDI	RBR concerto, IDRONAUT

For the bottom tracking observation, a WorkHorse Sentinel 600 kHz RDI was used. From the raw data measured by ADCPs, outliers at the 99% confidence intervals were excluded from analysis.

Appendix B. Unstructured Grid for FVCOM
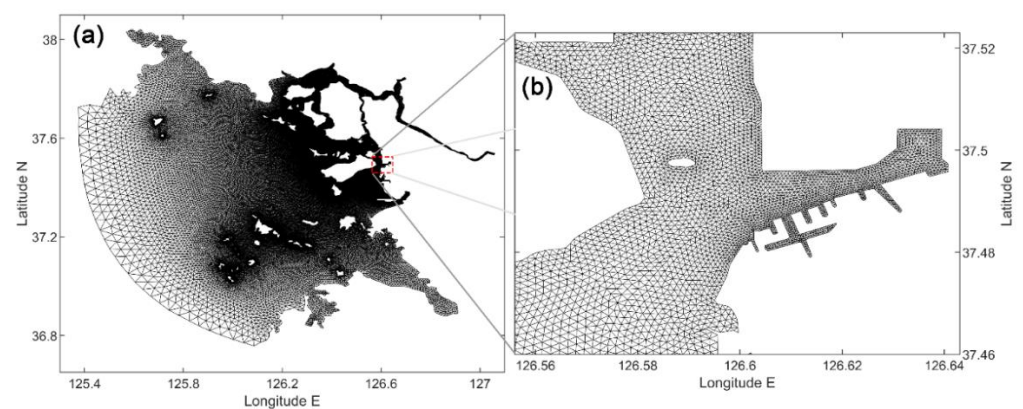
Figure A1. (**a**) Unstructured computational grid for Gyeonggi Bay; and (**b**) grid near the North Port.

References

1. Cheng, Z.; Jalon-Rójas, I.; Wang, X.; Liu, Y. Impacts of land reclamation on sediment transport and sedimentary environment in a macro-tidal estuary. *Estuar. Coast. Shelf Sci.* **2020**, *242*, 106861. [CrossRef]
2. van Maren, D.S.; van Kessel, T.; Cronin, K.; Sittoni, L. The impact of channel deepening and dredging on estuarine sediment concentration. *Cont. Shelf Res.* **2015**, *95*, 1–14. [CrossRef]
3. Park, K.; Wang, H.V.; Kim, S.-C.; Oh, J.-H. A Model Study of the Estuarine Turbidity Maximum along the Main Channel of the Upper Chesapeake Bay. *Estuaries Coasts* **2008**, *31*, 115–133. [CrossRef]
4. Ganju, N.; Schoellhamer, D. Calibration of an estuarine sediment transport model to sediment fluxes as an intermediate step for simulation of geomorphic evolution. *Cont. Shelf Res.* **2009**, *29*, 148–158. [CrossRef]
5. Uncles, R.J.; Stephens, J.A. Distributions of suspended sediment at high water in a macrotidal estuary. *J. Geophys. Res. Ocean.* **1989**, *94*, 14395–14405. [CrossRef]
6. Stoschek, O.; Zimmermann, C. Water Exchange and Sedimentation in an Estuarine Tidal Harbor Using Three-Dimensional Simulation. *J. Waterw. Port Coast. Ocean. Eng.* **2006**, *132*, 410–414. [CrossRef]
7. PIANC. *Minimising Harbor Siltation, Report No. 102-2008*; PIANC: Brussels, Belgium, 2008.
8. Juez, C.; Thalmann, M.; Schleiss, A.J.; Franca, M.J. Morphological resilience to flow fluctuations of fine sediment deposits in bank lateral cavities. *Adv. Water Resour.* **2018**, *115*, 44–59. [CrossRef]

9. Lee, G.H.; Shin, H.J.; Kim, Y.T.; Dellapenna, T.M.; Kim, K.J.; Williams, J.; Kim, S.Y.; Figueroa, S.M. Field investigation of siltation at a tidal harbor: North Port of Incheon, Korea. *Ocean Dyn.* **2019**, *69*, 1101–1120. [CrossRef]

10. Park, K.; Oh, J.-H.; Kim, H.-S.; Im, H.-H. Case Study: Mass Transport Mechanism in Kyunggi Bay around Han River Mouth, Korea. *J. Hydraul. Eng.* **2002**, *128*, 257–267. [CrossRef]

11. Gu, B.-H.; Woo, S.-B.; Kim, S. Improved Estuaries Salinity Stratification at Gyeonggi Bay Using Data Assimilation with Finite Volume Coastal Ocean Model (FVCOM). *J. Coast. Res.* **2019**, *91*, 416–420. [CrossRef]

12. Yoon, B.I.; Woo, S.B. The Along-channel Salinity Distribution and its Response to River Discharge in Tidally-dominated Han River Estuary, South Korea. *Procedia Eng.* **2015**, *116*, 763–770. [CrossRef]

13. Guerra-Chanis, G.E.; Reyes-Merlo, M.Á.; Díez-Minguito, M.; Valle-Levinson, A. Saltwater intrusion in a subtropical estuary. *Estuar. Coast. Shelf Sci.* **2019**, *217*, 28–36. [CrossRef]

14. Monismith, S.G.; Kimmerer, W.; Burau, J.R.; Stacey, M.T. Structure and Flow-Induced Variability of the Subtidal Salinity Field in Northern San Francisco Bay. *J. Phys. Oceanogr.* **2002**, *32*, 3003–3019. [CrossRef]

15. Bowen, M.M.; Geyer, W.R. Salt transport and the time-dependent salt balance of a partially stratified estuary. *J. Geophys. Res. Ocean.* **2003**, *108*, 3158. [CrossRef]

16. Oey, L.-Y. On Steady Salinity Distribution and Circulation in Partially Mixed and Well Mixed Estuaries. *J. Phys. Oceanogr.* **1984**, *14*, 629–645. [CrossRef]

17. Gong, W.; Shen, J. The Response of Salt Intrusion to Changes in River Discharge and Tidal Mixing During the Dry Season in the Modaomen Estuary, China. *Cont. Shelf Res.* **2011**, *31*, 769–788. [CrossRef]

18. Li, Y.; Liu, J. Salt intrusion and its controls in the macro-tidal Oujiang River Estuary, China. *Ocean Dyn.* **2020**, *70*, 1409–1420. [CrossRef]

19. Yoon II, B.; Woo, S.-B. Correlation between freshwater discharge and salinity intrusion in the Han River Estuary, South Korea. *J. Coast. Res.* **2013**, *65*, 1247–1252. [CrossRef]

20. Ralston, D.K.; Geyer, W.R.; Lerczak, J.A. Structure, variability, and salt flux in a strongly forced salt wedge estuary. *J. Geophys. Res. Ocean.* **2010**, *115*, C06005. [CrossRef]

21. Chen, C.; Liu, H.; Beardsley, R.C. An Unstructured Grid, Finite-Volume, Three-Dimensional, Primitive Equations Ocean Model: Application to Coastal Ocean and Estuaries. *J. Atmos. Ocean. Technol.* **2003**, *20*, 159–186. [CrossRef]

22. Chen, C.; Beardsley, R.; Cowles, G. *An Unstructured Grid, Finite-Volume Coastal Ocean Model: FVCOM User Manual*, 2nd ed.; Sea Grant College Program, Massachusetts Institute of Technology: Cambridge, MA, USA, 2006.

23. Egbert, G.D.; Erofeeva, S.Y. Efficient inverse modeling of barotropic ocean tides. *J. Atmos. Ocean. Technol.* **2002**, *19*, 183–204. [CrossRef]

24. Chen, C.; Beardsley, R.; Franks, P.J.S. A 3-D prognostic numerical model study of the Georges Bank ecosystem. Part I: Physical model. *Deep. Res. Part II Top. Stud. Oceanogr.* **2001**, *48*, 419–456. [CrossRef]

25. Cowles, G.W.; Lentz, S.J.; Chen, C.; Xu, Q.; Beardsley, R.C. Comparison of observed and model-computed low frequency circulation and hydrography on the New England Shelf.pdf. *J. Geophys. Res.* **2008**, *113*, C09015. [CrossRef]

26. Komen, G.J.; Hasselmann, K. On the Existence of a Fully Developed Wind-Sea Spectrum. *J. Phys. Oceanogr.* **1984**, *14*, 1271–1285. [CrossRef]

27. Madsen, O.S.; Poon, Y.K.; Graber, H.C. Spectral wave attenuation by bottom friction: Theory. In Proceedings of the 21st Conference on Coastal Engineering, Torremolinos, Spain, 29 January 1988; Edge, B.L., Ed.; ASCE: Reston, VA, USA; pp. 492–504.

28. Qi, J.; Chen, C.; Beardsley, R.C.; Perrie, W.; Cowles, G.W.; Lai, Z. An unstructured-grid finite-volume surface wave model (FVCOM-SWAVE): Implementation, validations and applications. *Ocean Model.* **2009**, *28*, 153–166. [CrossRef]

29. Winterwerp, J. Reducing Harbor Siltation. I: Methodology. *J. Waterw. Port Coast. Ocean. Eng.* **2005**, *131*, 258–266. [CrossRef]